Atmos. Chem. Phys. Discuss., 15, 1573–1615, 2015
www.atmos-chem-phys-discuss.net/15/1573/2015/
doi:10.5194/acpd-15-1573-2015


Atmospheric Chemistry and Physics
Discussions
Open Access



# Ice phase in altocumulus clouds over Leipzig: remote sensing observations and detailed modelling

**M. Simmel, J. Bühl, A. Ansmann, and I. Tegen**

TROPOS, Leibniz Institute for Tropospheric Research, Permoser Str. 15, 04318 Leipzig, Germany

Received: 19 December 2014 – Accepted: 26 December 2014 – Published: 19 January 2015

Correspondence to: M. Simmel (simmel@tropos.de)

Published by Copernicus Publications on behalf of the European Geosciences Union.







Ice phase in altocumulus clouds over Leipzig

M. Simmel et al.

## Abstract

The present work combines remote sensing observations and detailed cloud modeling to investigate two altocumulus cloud cases observed over Leipzig, Germany. A suite of remote sensing instruments was able to detect primary ice at rather warm temperatures of $-6\,^{\circ}$C. For comparison, a second mixed phase case at about $-25\,^{\circ}$C is introduced. To further look into the details of cloud microphysical processes a simple dynamics model of the Asai–Kasahara type is combined with detailed spectral microphysics forming the model system AK-SPECS. Vertical velocities are prescribed to force the dynamics as well as main cloud features to be close to the observations. Subsequently, sensitivity studies with respect to ice microphysical parameters are carried out with the aim to quantify the most important sensitivities for the cases investigated. For the cases selected, the liquid phase is mainly determined by the model dynamics (location and strength of vertical velocity) whereas the ice phase is much more sensitive to the microphysical parameters (ice nuclei (IN) number, ice particle shape). The choice of ice particle shape may induce large uncertainties which are in the same order as those for the temperature-dependent IN number distribution.

## 1 Introduction

Altocumulus clouds observations by Bühl et al. (2013) show the typical feature with a maximum of liquid water in the upper part of the cloud and an ice maximum in the lower part of the cloud, mostly below liquid cloud base down in the virgae. The observations with the highest temperatures are close to the limit at which the best atmospheric ice nuclei are known to nucleate ice in the immersion mode. This can only be attributed the aerosol particles which are formed out of or at least contain biological material such as bacteria (Hartmann et al., 2013), fungi, or pollen. This is corroborated by the review of Murray et al. (2012) stating that only biological particles are known to form ice above $-15\,^{\circ}$C. However, these observations are from laboratory studies and it is still unclear





ACPD
15, 1573–1615, 2015

whether or to which extent these extremely efficient ice nuclei are abundant in atmosphere, especially above the boundary layer. One idea is that freezing is caused by soil dust with biological particles dominating the freezing behaviour (O'Sullivan et al., 2014). Seeding from ice clouds above can be excluded for the cases presented; however, preconditioning of ice nuclei (IN) could be a reason for these high ice activation temperatures.

Ice nucleation still is a large source of uncertainity in cloud modeling. Recently, several studies use combinations of vertically fine resolved models with rather detailed representation of the ice nucleation processes. Often, wave clouds are used as comparison since they represent rather ideal conditions when they are not influenced by ice seeding from layers above. Field et al. (2012) apply a 1-D kinematic model with bulk microphysics but prognostic IN. Eidhammer et al. (2010) use a Langrangian parcel model for the comparison of the ice nucleation schemes of Phillips et al. (2008) and DeMott et al. (2010) under certain constraints. A 1-D column model with a very detailed 2-D spectral description of liquid and ice phase is employed by Dearden et al. (2012). Sun et al. (2012) use a 1.5-D model with spectral microphysics for shallow convective clouds for a sensitivity study of immersion freezing due to bacteria and its influence on precipitation formation.

Most ice microphysics descriptions in models lack from the fact that ice nuclei are not represented as a prognostic variable. These models diagnose the number of ice particles based on thermodynamical parameters such as temperature and humidity (Meyers et al., 1992) and are, therefore, not able to consider whether IN were already activated at previous time steps in the model.

The paper is structured as follows. Section 2 describes the remote sensing observations of two altocumulus cloud cases above Leipzig. The dynamical model as well as the process descriptions and initial data used for this study are specified in Sect. 3. Section 4 refers to changes in the dynamic parameters of the model to identify base cases. The results for the sensitivity studies with respect to the microphysical parameters are presented in Sects. 5 and 6 closes with a discussion of the results.

## 2 Remote sensing observations

Altocumulus and altostratus clouds are regularly observed with the Leipzig Aerosol and Cloud Remote Observations System (LACROS) at TROPOS. LACROS combines the capabilities of Raman/depolarization lidar (Althausen et al., 2009), a MIRA-35 cloud radar (Bauer-Pfundstein and Görsdorf, 2007), a Doppler lidar (Bühl et al., 2012), a microwave radiometer, a sun-photometer and a disdrometer to measure height-resolved properties of aerosols and clouds. The Cloudnet framework (Illingworth et al., 2007) is used to derive microphysical parameters like liquid-water content (Pospichal et al., 2012) or ice-water content (Hogan et al., 2006). The following two cases have been selected to illustrate this variety and to serve as examples to be compared to model results.

### 2.1 Case 1: warm mixed-phase cloud

One of the warmest mixed-phase clouds within the data set was observed on 17 September 2011 between 00:00 and 00:22 UTC (see Fig. 1). The liquid part of the cloud extends from about 4250 to 4450 m height at temperatures of about $-6\,^{\circ}$C according to the GDAS reanalysis data for Leipzig. Liquid water path (LWP) measured by a microwave radiometer varies between 20 and 50 $\mathrm{g\,m^{-2}}$ (mostly about 25 $\mathrm{g\,m^{-2}}$) whereas ice water path (IWP) is only slightly above the detection limit of about 0.01 $\mathrm{g\,m^{-2}}$ implying a rather large uncertainty with correspondingly large error bars. Virgae (falling ice) are observed down to about 3000 m, which is close to the $0\,^{\circ}$C level. Vertical windspeeds range from about $-1.5$ to 1.0 $\mathrm{m\,s^{-1}}$ with pdf maxima at $-0.5$ and 0.5 $\mathrm{m\,s^{-1}}$, respectively (Fig. 2).

### 2.2 Case 2: colder mixed-phase cloud

A much colder case could be observed on 2 August 2012 between 21:00 and 21:40 UTC (see Fig. 3). Liquid water was measured around 7500 m at about $-25\,^{\circ}$C





ACPD
15, 1573–1615, 2015

with an LWP between 10 and 30 $\mathrm{g\,m^{-2}}$. As can be expected due to the lower temperature, the ice phase was much more massive than in case 1 and reached down to about 5500 m with an IWP of about 1–10 $\mathrm{g\,m^{-2}}$. Vertical wind speeds were in the same range as for the warmer case described above (Fig. 4).

## 3 Model description and initialization

For the model studies an Asai–Kasahara type model is used (Asai and Kasahara, 1967). The model geometry is axisymmetric and consists of an inner and an outer cylinder. The vertical resolution is constant with height and is chosen to be $\Delta z = 25$ m to give a sufficient resolution of the cloud layer and to roughly match the vertical resolution of the observations. In contrast to a parcel model, the vertically resolved model grid allows for a description of hydrometeor sedimentation. This is important especially for the fast growing ice crystals to realistically describe their interaction with the vapor and liquid phase (Bergeron–Findeisen process).

The cloud microphysics is described by the mixed-phase spectral microphysics module SPECS (Simmel and Wurzler, 2006; Diehl et al., 2006). SPECS provides a joint spectrum for the liquid phase (soluble wetted aerosol particles as well as cloud and rain drops) and one spectrum for the ice phase.

### 3.1 Description of ice microphysics

In the following, the differences in the description of the microphysics compared to Diehl et al. (2006) are described.

#### 3.1.1 Immersion freezing

For this study, immersion freezing is assumed to be the only primary ice formation process. Since during the above mentioned observations no measurements of the IN are available, the parameterization of DeMott et al. (2010) is used assuming that all





ACPD
15, 1573–1615, 2015

IN are active in the immersion freezing mode. The parameterization of DeMott et al. (2010) is based on an empirical relation of IN and the number of aerosol particles with radii > 250 nm ($N_{\mathrm{AP},\, r>250\,\mathrm{nm}}$). As base case $N_{\mathrm{AP},\, r>250\,\mathrm{nm}} = 10^5\,\mathrm{kg}^{-1}$ air is used as input data for the parameterization resulting in about 0.01 active IN $\mathrm{L}^{-1}$ for −6 °C (case 1) and about 0.5 IN $\mathrm{L}^{-1}$ for −25 °C (case 2), respectively, at standard conditions. This corresponds to a relatively low number of larger aerosol particles.

For the potential IN a prognostic temperature resolved field with 20 temperature bins with a resolution of 1 K is introduced into SPECS. It ranges from −5 to −25 °C to cover the temperature range for the selected cases and can easily be changed for other case studies. This is a simplified version of the method used by Fridlind et al. (2007). The potential IN field is initially defined in every grid cell (layer) and is transported vertically with the given up-/downdrafts and horizontally exchanged between inner and outer cylinder in the same way as the other hydrometeor fields (drops and ice crystals). Immersion freezing occurs as soon as liquid drops above a certain size limit are present and the temperature of a certain potential IN bin is reached. Then the respective amount of drops freezes (if available) instantaneously and is transferred from the liquid to the frozen spectrum. If more drops larger than the size threshold of 10 µm than active IN are present, the IN are distributed evenly over all drop size bins above the threshold value. If ice crystals melt below the freezing level, they contribute to the potential IN field at that level.

### 3.1.2 Ice particle shape

It is well known that ice particle shape highly influences water vapor deposition (described by changing the capacitance of the particle) as well as terminal fall velocity of the ice particle. Therefore, instead of the previously chosen spherical ice particle shape, ice particles now can be prescribed as hexagonal columns or plates. The aspect ratio can be either constant for all size bins or be changed with size following the approach of Mitchell (1996). Typically, with increasing particle size, the deviation from an uniform aspect ratio increases. In our simulations, a constant uniform aspect ratio (ar = 1) is used as base case. From Mitchell (1996) the size-varying aspect ratios for plates and columns are used for sensitivity studies.

The (relative) capacitance needed for the calculation of deposition growth of the ice crystals is modeled using the method of Westbrook et al. (2008) for the aspect ratios given above. Ice crystal terminal fall velocities are calculated according to Heymsfield and Westbrook (2010) using the same aspect ratios.

## 3.2 Model initialization

### 3.2.1 Thermodynamics

The Asai–Kasahara model has to be initialized with vertical profiles of temperature and dewpoint temperature either from reanalysis data (here GDAS) or radiosonde profiles from nearby stations (here Meiningen, Thuringia). For case 1, profiles from both methods show a similar general behaviour but the radiosonde profile of Meiningen measured at 00:00 UTC is used since it provides a finer vertical resolution than the GDAS reanalysis data. However, for case 2 the Meiningen RS profile misses the humidity layer at the level where the clouds were observed and, therefore, GDAS reanalysis data for Leipzig at 21:00 UTC were chosen. Finally, both profiles used show a sufficiently humid layer where the clouds were observed, so that lifting of these layers lead to supersaturation and subsequent cloud formation.

In contrast to other Asai–Kasahara model studies, updrafts are not initialized by a heat and/or humidity pulse in certain layers for a given period of time. Instead, vertical velocity (updrafts and downdrafts) in the inner cylinder is prescribed at cloud level ranging from $h_{bot}$ to $h_{top}$. The center of this interval is given by $h_{mid} = (h_{top} + h_{bot})/2$ and its half-depth by $h_{depth} = (h_{top} - h_{bot})/2$. $h_{bot}$ ranges from 3800 to 4100 m for case 1 and from 7000 to 7300 m for case 2. The respective values for $h_{top}$ are 4500 and 7700 m.





ACPD
15, 1573–1615, 2015

The vertical dependency (compare Fig. 5, left) is given by

$$f_h(h) = \frac{h_{\mathrm{depth}}^2 - (h - h_{\mathrm{mid}})^2}{h_{\mathrm{depth}}^2} \quad \text{for} \quad h_{\mathrm{bot}} \le h \le h_{\mathrm{top}} \tag{1}$$

resulting in the time- and height-dependent function

$$w(h,t) = w_{\mathrm{mid}}(t) f_h(h) \quad \text{for} \quad h_{\mathrm{bot}} \le h \le h_{\mathrm{top}} \tag{2}$$

and $w(h,t) = 0$ otherwise, defining $w_{\mathrm{mid}}(t)$ as the updraft velocity at $h_{\mathrm{mid}}$. In order to match the observed wind field distributions rather closely, $w_{\mathrm{mid}}(t)$ is chosen as a stochastic function

$$w_{\mathrm{mid}}(t) = w_{\mathrm{ave}} + f_{\mathrm{scal}} \frac{\delta(t)^3}{|\delta(t)|} \tag{3}$$

where $w_{\mathrm{ave}}$ is the average ("large-scale") updraft velocity at $h_{\mathrm{mid}}$ varying between 0.1 and $0.4\,\mathrm{m\,s^{-1}}$, $f_{\mathrm{scal}}$ is the scaling factor determining the range of updraft velocities (chosen as $4\,\mathrm{m\,s^{-1}}$ to obtain a difference of minimum and maximum velocity of $2\,\mathrm{m\,s^{-1}}$), and $\delta(t)$ is a random number ranging from $-0.5$ to $+0.5$ obtained from a linear stochastic process provided by FORTRAN. After 30 s model time a new $\delta(t)$ is created. Different realizations of the stochastic process are tested (see below). E.g., $w_{\mathrm{mid}}(t)$ ranges from $-0.7$ to $1.3\,\mathrm{m\,s^{-1}}$ if $w_{\mathrm{ave}} = 0.3\,\mathrm{m\,s^{-1}}$ and $f_{\mathrm{scal}} = 4\,\mathrm{m\,s^{-1}}$ as it is shown in the temporal evolution and the histogram in Fig. 5.

Due to the height dependent vertical velocity $w$, a horizontal transport velocity $u_k$ (exchange between inner and outer cylinder) is induced in the Asai–Kasahara formulation for a given model layer $k$.

$$u_k = -\frac{w_{k+\frac{1}{2}}\rho_{k+\frac{1}{2}} - w_{k-\frac{1}{2}}\rho_{k-\frac{1}{2}}}{f_r \Delta z \rho_k} \tag{4}$$





ACPD
15, 1573–1615, 2015

Ice phase in altocumulus clouds over Leipzig

M. Simmel et al.

Full indices $k$ indicate values at level centers whereas half indices ($k+\frac{1}{2}$, $k+\frac{1}{2}$) describe values at level interfaces. $f_r = 2/r_i$ is a geometry parameter with the radius $r_i = 1000$ m of the inner cylinder.

The prescribed velocity field leads to the following effects (all descriptions are related to the inner cylinder if not stated otherwise explicitly):

- In the updraft phase: in the upper part (between $h_{\text{mid}}$ and $h_{\text{top}}$) of the updraft, mixing occurs from the inner to the outer cylinder whereas in the lower part (between $h_{\text{low}}$ and $h_{\text{mid}}$), horizontal transport is from the outer cylinder into the inner one
- For downdrafts it is the other way: this means that below $h_{\text{mid}}$ drops and ice particles are transported from the inner cylinder to the outer one and are therefore removed from the inner cylinder
- below $h_{\text{low}}$ or above $h_{\text{top}}$, no horizontal exchange takes place.

The question arises to which extent this dynamical behaviour reflects the real features of the observed clouds and whether this is critical for the topics aimed at in this study.

Prescribing vertical velocity in any way also means that a feedback of microphysics on dynamics due to phase changes (e.g., release of latent heat for condensing water vapor or freezing/melting processes) is not considered by the model.

#### 3.2.2 Aerosol distribution

Since no in situ aerosol measurements are available, literature data is used. The Raman lidar observations do not show any polluted layers for both cases; therefore data from LACE98 (Petzold et al., 2002) are used. For case 1 values for the lower free troposphere (M6), for case 2 those from the upper free troposphere (M1) are used (see Petzold et al., 2002, Table 6).





ACPD
15, 1573–1615, 2015

Ice phase in altocumulus clouds over Leipzig

M. Simmel et al.

## 4 Model results: dynamics

In a first step, the aim is to achieve a sufficient agreement concerning macroscopic cloud features as well as (liquid phase) microphysics as far as they were observed. The following parameters describing model dynamics (updraft velocity) are varied to identify a "best case" which in the second step can be used to perform sensitivity studies with respect to (ice) microphysics (see also Tables 1 and 2).

- $h_{\text{low}}$: ranging from 3800 to 4100 m for the warmer and from 7000 to 7300 m for the colder case. This parameter influences the vertical cloud extent and, therefore, liquid water content and liquid water path.
- $w_{\text{ave}}$: ranging from 0.1 to 0.4 $\text{m s}^{-1}$. Higher average updraft also leads to higher LWC. Due to the lateral mixing processes the model setup requires a positive updraft velocity in average to form and maintain clouds.
- $\delta$: Four different realizations of the stochastic process are used. This influences the timing of the cloud occurence as well as LWC and LWP but not systematically.

All model results shown refer to the inner cylinder.

### 4.1 Case 1: warm mixed-phase cloud

Figures 6 and 8 show time-height plots of the liquid (contours, linear scale) and ice (colours, logarithmic scale) water mixing ratio for case 1 illustrating the cloud sensitivity with respect to variation of cloud base ($h_{\text{bot}}$), average vertical updraft ($w_{\text{ave}}$), and the realization of the stochastic process, respectively. Liquid clouds form in the updraft regions (cp. Fig. 5) whereas in the downdrafts the liquid phase vanishes at least partly. Ice forms mainly at cloud base and immediately starts to sediment. Due to the supersaturation with respect to ice even below liquid cloud base, ice particles still grow while sedimenting, reaching their maximum size before, finally, subsaturated regions are reached and evaporation sets in. Figures 7 and 9 show the time evolution of liquid





ACPD
15, 1573–1615, 2015

(lower panel) and ice water path (upper panel) for the same parameters varied, reflecting the same temporal patterns. Table 1 summarizes the maximum values for liquid and ice water mixing ratio (LWMR/IWMR), liquid and ice water path (LWP/IWP) as well as cloud droplet and ice particle number concentration (CDN/IPN) for all dynamics sensitivity runs for case 1.

One can clearly observe, that a lower $h_{bot}$ (Fig. 6) results in a lower cloud base, larger vertical cloud extent as well as more liquid water. The same trend with similar intensity is observed for the ice phase (see also Fig. 7). However, the values of the two maxima of the condensed phase after about 15–20 min and about 40 min model time are quite different. The first maximum is more pronounced for the ice phase whereas the second one is larger for the liquid phase. While the liquid phase is dominated by the updraft velocity (see Fig. 5) the ice phase additionally depends on IN supply. In the first ice formation event at 15 min, all IN active at the current temperature actually form ice leading to an IN depletion. Due to the horizontal exchange with the outer cylinder the IN reservoir is refilled, but only to a certain extent when the second event after 40 min sets in. Due to the limited IN supply the second ice maximum is weaker than the first one. The stochastic velocity fluctuations cause fluctuations in relative humidity, which are directly reflected by the liquid phase parameters whereas the ice phase generally reacts much slower. Sensitivity of CDN and IPN with respect to change of $h_{bot}$ does not seem to be systematic.

Increasing the average updraft velocity $w_{ave}$ leads to a similar increase of liquid water and ice as lowering $h_{bot}$ (see Figs. 8, upper panel and 9, left). This can be expected since more water vapor flows through the cloud and is able to condense. However, a certain limit seems to be reached for W_w04, since the increase of LWP slows down (see maximum value at 40 min in Fig. 9, left). This is due to the enhanced horizontal exchanged following eq. (4). Additionally, the stronger updrafts allow the ice particles a longer presence time in the vicinity of the cloud and, therefore, an enhanced growth at comparably high supersaturation with respect to ice before sedimentation sets in at larger sizes. This also leads to an accumulation of ice particles and, therefore, to





ACPD
15, 1573–1615, 2015

a higher IPN. Surprisingly, CDN only depends weakly and not systematically on $w_{ave}$ which is in contrast to the typical enhancement of CDN with increasing updraft velocities.

Figures 8 (lower panel) and 9 (right) show that different realizations of the stochastic process (as explained above in Sect. 3.2.1) lead to different temporal cloud evolutions. However, differences in maximum LWP and LWMR are much smaller than those discussed above. Variations in maximum IWP and IWMR as well as CDN and IPN are in the range of about 30 %. This is also true for average LWP ranging from 18 g m$^{-2}$ for W_r1 to 26 g m$^{-2}$ for W_r3. However, despite the different maxima and temporal evolutions of IWP, average IWP is almost identical for the different stochastic realizations (0.023 g m$^{-2}$). This shows that changing the stochastic realization influences cloud evolution in detail (timing) but does not change the overall picture.

With maximum values between 17 and 57 g m$^{-2}$ the modeled liquid water path is in the same range as the observed values (20–50 g m$^{-2}$), especially for the "wetter" runs (smaller $h_{bot}$, larger $w_{ave}$). Average LWP typically is about half (40–60 %) of the maximum value for most of the runs which also fits well into the observations. Ice forms within the liquid layer and sediments to about 3800 m for most runs which is less than for the observations. The (maximum) modeled ice mixing ratio is in the same order of magnitude as the observed one (about 10$^{-7}$ kg m$^{-3}$). The same holds for the ice water path with values of about 0.01 g m$^{-2}$ for both, model and observation. For the other values, no observational data is available for comparison.

### 4.2 Case 2: colder mixed-phase cloud

Due to the colder temperatures of case 2 much more ice is produced than in case 1 (see Figs. 10–13 as well as Table 2). Therefore, the virgae reach down to more than 1500 m below liquid cloud base which is in concordance with the observations. The principal behaviour with respect to the sensitivity parameters is similar as in case 1: the liquid phase is enhanced by either decreasing $h_{bot}$ or increasing $w_{ave}$, showing the "saturation" effect slightly more pronounced as in case 1. Different stochastic realizations





ACPD
15, 1573–1615, 2015

only weakly influence the maximum and average values of the liquid phase but change the timing of occurence. Generally, the variability of the ice phase is weaker than in case 1. The different stochastic realizations show the highest variability in IWMR and IWP. Different variations of $h_{bot}$ show almost identical IWPs, whereas changing $w_{ave}$ at least slighly influences maximum IWMR and IWP, which again can be attributed to the ice particle accumulation in the updraft. Liquid water path is smaller than in case 1 and reaches maximum values between 10 and 43 $\mathrm{g\,m^{-2}}$ which well covers the observed maximum value of about 20 $\mathrm{g\,m^{-2}}$. Cloudnet observations show an IWC of $10^{-7}$–$10^{-5}$ $\mathrm{kg\,m^{-3}}$ which is an increase by a factor of 10–100 compared to case 1. Similar values are obtained by the model results underlining the strong temperature dependency of the ice nucleation process.

## 5 Sensitivity studies

In the previous section it could be shown that dynamical parameters can be chosen in a way that the model results (in terms of LWP, IWP as well as cloud geometry) are in good agreement with the observations. This allows to perform sensitivity studies with respect to cloud microphysics. To cover the proper sensitivities we have to answer the question which microphysical parameters are expected to have a large influence on mixed phase microphysics and are rather uncertain to be estimated. This leads to (temperature-dependent) IN number ($N_{IN}$) which directly influences ice particle number but mostly is poorly known. To be consistent with the freezing parameterization of the model, $N_{IN}$ is varied by changing $N_{AP,\,r>250\,\mathrm{nm}}$ which additionally is easier to observe in most cases. A second parameter is the shape of the ice particles which does not influence the primary freezing process but the subsequent growth by water vapor deposition onto existing ice particles and, therefore, the total ice mass produced. Their relative importance shall be quantified and also be compared to the influence of dynamics discussed above.





ACPD
15, 1573–1615, 2015

## 5.1 IN number

Changing $N_{\text{AP},\, r>250\,\text{nm}}$ leads to a temperature-dependent change of IN number which is relatively small for warmer conditions. However, the effect increases with decreasing temperature. This is illustrated by the following numbers. The parameterization of DeMott et al. (2010) gives about 0.009 active IN $\text{L}^{-1}$ at standard conditions ($N_{\text{IN}}$) when $N_{\text{AP},\, r>250\,\text{nm}} = 10^5\,\text{kg}^{-1}$ at $T = -5\,^\circ\text{C}$. A tenfold increase to $N_{\text{AP},\, r>250\,\text{nm}} = 10^6\,\text{kg}^{-1}$ results in about 0.012 active IN $\text{L}^{-1}$ which is a rise of only about 35 %. For $T = -7\,^\circ\text{C}$, IN number rises by about 65 % for a tenfold increase of $N_{\text{AP},\, r>250\,\text{nm}}$. This shows that for those rather warm temperatures considered for case 1, a massive change in $N_{\text{AP},\, r>250\,\text{nm}}$ leads to relatively small changes in $N_{\text{IN}}$ and only a small effect on the ice phase can be expected. This is confirmed by Fig. 14 (left) showing liquid and ice water mixing ratios for W_in6. Ice mass is enhanced by less than 60 % for W_in6 and by about 160 % for W_in7 which is consistent for the given temperature range (see Table 3). Similar values are obtained for the change in IPN. This directly leads to the conclusion that the individual ice particles grow independently from each other. Their individual growth history is (in contrast to drop growth) only influenced by thermodynamics as long as their number is low enough which seems to be the case here.

This is confirmed by Fig. 15 showing drop and ice particle size distributions at the time when the maximum IWP is reached (16 min for case 1, 17 min for case 2). For case 1 (upper panel), the liquid phase (contours) is unaffected by the IN enhancement. Despite the increase of ice particle number and mass the shape of the ice particle size distribution (colors) is not changed. The smallest ice particles can be observed at three discrete height (and temperature) levels caused by the temperature resolved parameterization of the potential IN described in Sect. 3.1.1. In reality this part of the spectrum showing rather freshly nucleated and fast growing ice particles should be continuous over the height range from about 4100 to 4400 m. Nevertheless, the total number of ice particles formed is described correctly.





ACPD
15, 1573–1615, 2015

One can conclude that increasing IN number therefore increases ice particle number as well as ice mass proportionally. Generally, the ice mass remains small and the liquid phase is not affected by the ice mass increase. Those results are supported by Fig. 16 (left) showing an unchanged LWP and a proportionally growing IWP for increased IN numbers.

For the colder case 2 the parameters are varied in the same way. However, one big difference is that a tenfold increase of $N_{\mathrm{AP},\,r>250\,\mathrm{nm}}$ at $T = -25\,^{\circ}\mathrm{C}$ results in a much larger change in active IN. Their number rises by 300 % from about 0.5 $\mathrm{L}^{-1}$ to about 2 $\mathrm{L}^{-1}$ following the parameterization. This is reflected by the IPN values in Table 4. Figure 14 (right) and Table 4 show that ice mass increases in such a way that liquid water is depleted partially (C_in6 by about 50 %) or almost totally (C_in7) due to the Bergeron–Findeisen process. Compared to C_base, ice is enhanced by a factor of 3–4 for C_in6 and about 10 for C_in7 whereas IPN increases by a factor of 12. This can also be seen in the IWP (Fig. 16, right, red lines) showing a limited increase for C_in7, especially for the first maximum after 17 min. This means that the results for C_in6 are still consistent with an independent growth of the individual ice particles (as described above) despite the relatively high ice occurence.

This is verified by the size distributions in Fig. 15 (lower panel). As in case 1 the ice particle size distributions only differ by the number/mass, but not by shape. Additionally, the decrease in the liquid phase is reflected also in the drop spectrum showing a more shallow liquid part of cloud as well as droplet distribution shifted to smaller sizes.

However, for C_in7 the ice particles compete for water vapor which becomes clear from (i) the depletion of liquid water (resulting in a lower supersaturation with respect to ice) and (ii) the ice mass enhancement factor being below the value expected from the ice nucleation parameterization and below that of IPN. This means that despite the higher number of IN and, therefore, ice particles, the amount of ice is limited by the thermodynamic conditions which results in the production of more but smaller ice particles, similar to the Twomey effect for drop activation.





ACPD
15, 1573–1615, 2015

Ice phase in altocumulus clouds over Leipzig

M. Simmel et al.

## 5.2 Ice particle shape

As discussed previously, for most of the cases (except for C_in7) changing the parameters in the section above does neither influence the ice particles themselves nor their individual growth. Additionally, due to their low number, there is almost no competition of the ice particles for water vapor, and, therefore, ice water content scales linearly with ice particle number. In contrast to this, changing the ice particle shape from quasi-spherical (ar = 1) to columns or plates with size-dependent axis ratios deviating from unity results in an increase of water vapor deposition on the individual ice particles leading to enhanced ice water content due to larger individual particles when ice particle numbers remain unchanged. This is due to (i) enhanced relative capacitance resulting in faster water vapor deposition and (ii) lower terminal velocities of the ice particles leading to longer residence times in vicinity of conditions with supersaturation with respect to ice.

Figure 17 (left) shows the results for the runs using hexagonal columns (W_col) as prescribed ice particle type. Compared to the previous results (W_base, W_in6, W_in7) more ice mass is produced (see Table 3) but still the liquid part of the cloud remains unaffected (compare also LWP and IWP in Fig. 16, left). Similar results are obtained for the assumption of plate-like ice particles (W_pla). The mass increase results from the larger ice particle size due to the reasons discussed above which can be seen from Fig. 18 showing the size distributions for W_col at different times. On the upper left panel W_col is shown after 16 min corresponding to Fig. 15. Compared to W_base, larger ice particles are produced leading to more ice mass (equivalent radius up to 300 µm compared to 189–238 µm for the base case). Additionally, due to the lower fall speed of the columns (1.03 $\mathrm{m\,s^{-1}}$ vs. 1.75–2.24 $\mathrm{m\,s^{-1}}$), the maximum of the ice is at about 4200 m compared to 4100 m for the base case. On the upper right panel, size distributions after 21 min are shown corresponding to the IWP maximum of W_col. Ice particles have grown larger (equivalent radius up to 378 µm, length of the columns increases from about 3 to 4.5 mm) and sedimentation has developped further





ACPD
15, 1573–1615, 2015

with increasing terminal velocity ($1.13\,\mathrm{m\,s^{-1}}$). Similar results are obtained for plates (W_pla) with terminal velocities of $0.89$–$1.21\,\mathrm{m\,s^{-1}}$, equivalent radii of 300–476 µm and maximum dimension of 1.8–3.2 mm.

The lower terminal velocity of columns and plates despite their larger size is leading to the stronger tilting of the virgae. Additionally, ice particle number IPN is enhanced by about 30 % although ice nucleation is identical to W_base. This can be attributed to the lower fall velocities, too, leading to an accumulation of ice particles. The differences between W_col and W_pla are caused by both, the higher relative capacitances of and lower terminal fall velocities of plates compared to columns (at least when their axis ratios are chosen following Mitchell, 1996).

For case 2 (C_col and C_pla), the liquid water reduction due to the Bergeron–Findeisen process is similar to C_in6 (see Fig. 17, right, and Table 4). In contrast to the respective case 1 runs, less ice is produced than for C_in7. The tilting of the virgae is not as strong as in W_col which is due to the larger ice particle sizes leading to higher terminal fall velocities ($1.43$–$1.60\,\mathrm{m\,s^{-1}}$). Additionally, the lower air density leads to an increase of terminal velocity of more than 10 % independently from shape. Figure 18 (lower panels) show the size distributions for C_col at different times. Due to the longer growth time larger individual ice particles than in case 1 are produced (equivalent radius up to 600 µm compared to 300 µm for the base case).

To decide whether independent ice particle growth or competition occurs, further runs with less IN (C_col_in4 and C_pla_in4) are discussed (see Fig. 16, right). IWMR and IWP of these runs (in4) are about one third of the values of the respective runs with more IN (in5). For ice particle number, a factor of slightly more than three occurs which means that a weak competition for water vapor occcurs for C_col and C_pla resulting in slightly smaller individual ice particles compared to C_col_in4 and C_pla_in4.





ACPD
15, 1573–1615, 2015

## 6 Conclusions

The model system AK-SPECS was applied to simulate dynamical and microphysical processes within altocumulus clouds. Sensitivity studies on relative contributions on cloud evolution as well as comparisons to observations were made.

Variation of the dynamic parameters as it was done in Sect. 4 leads to systematic differences mainly in the liquid phase (LWMR, LWP) which can easily be explained. More liquid water is produced when either cloud base is lowered (corresponding to a larger vertical cloud extent) or vertical wind velocity is increased. However, the effects of the dynamics on the ice phase are surprisingly small, at least smaller than those on the liquid phase. Increasing vertical velocity leads to an accumulation of the smaller ice particles in the enhanced updraft.

On the other hand, much larger differences in terms of IWMR and IWP were found when microphysical parameters like IN number or ice particle shape were varied under identical dynamic conditions. This is valid for both cases studied. However, at least for the ice nucleation parameterization used, sensitivity of IN number strongly increased with decreasing temperature.

This means that relatively large differences concerning the ice phase can only be reached when either IN number differs considerably or ice particle shape is different (which should not be the case for relatively similar thermodynamical conditions). After Fukuta and Takahashi (1999) for case 1 with temperatures of about $-6\,^{\circ}$C column-like ice particles with ar = 0.1 could be expected (corresdponding to W_col) whereas for case 2 $T < -24\,^{\circ}$C hexagonal particles with ar = 1 are most likely (e.g., C_base). Those ice shapes were observed in laboratory studies at water saturation which was also valied for the observed cases when ice formed by immersion freezing within the liquid layer of the cloud. These ice shapes can also explain why a depletion of the liquid phase was not observed in case 2 as it was predicted by the sensitivity studies using either columns or plates as prescribed shape. Generally, the liquid phase is affected considerably only when enough ice particles are present which typically is the case





ACPD
15, 1573–1615, 2015

for cold conditions with a sufficient amount of IN and fast growing ice particle shapes (most effective for large deviations from spherical shapes).

*Acknowledgements.* Funding by the Deutsche Forschungsgemeinschaft DFG project UDINE.

## References

Althausen, D., Engelmann, R., Baars, H., Heese, B., Ansmann, A., Müller, D., and Komppula, M.: Portable Raman lidar PollyXT for automated profiling of aerosol backscatter, Extinction, and Depolarization, J. Atmos. Ocean. Tech., 26, 2366–2378, doi:10.1175/2009JTECHA1304.1, 2009. 1576

Asai, T. and Kasahara, A.: A theoretical study of compensating downward motions associated with cumulus clouds, J. Atmos. Sci., 24, 487–496, doi:10.1175/1520-0469(1967)024<0487:ATSOTC>2.0.CO;2, 1967. 1577

Bauer-Pfundstein, M. R. and Görsdorf, U.: Target separation and classification using cloud radar doppler-spectra, in: Proceedings of the 33rd Conference on Radar Meteorology, 11B.2, August 2007, Cairns, Australia, 2007. 1576

Bühl, J., Engelmann, R., and Ansmann, A.: Removing the laser-chirp influence from coherent doppler lidar datasets by two-dimensional deconvolution, J. Atmos. Ocean. Tech., 29, 1042–1051, doi:10.1175/JTECH-D-11-00144.1, 2012. 1576

Bühl, J., Ansmann, A., Seifert, P., Baars, H., and Engelmann, R.: Toward a quantitative characterization of heterogeneous ice formation with lidar/radar: comparison of CALIPSO/CloudSat with ground-based observations, Geophys. Res. Lett., 40, 4404–4408, doi:10.1002/grl.50792, 2013. 1574

Dearden, C., Connolly, P. J., Choularton, T., Field, P. R., and Heymsfield, A. J.: Factors influencing ice formation and growth in simulations of a mixed-phase wave cloud, Journal of Advances in Modeling Earth Systems, 4, M10001, doi:10.1029/2012MS000163, 2012. 1575

DeMott, P. J., Prenni, A. J., Liu, X., Kreidenweis, S. M., Petters, M. D., Twohy, C. H., Richardson, M. S., Eidhammer, T., and Rogers, D. C.: Predicting global atmospheric ice nuclei distributions and their impacts on climate, P. Natl. Acad. Sci. USA, 107, 11217–11222, doi:10.1073/pnas.0910818107, 2010. 1575, 1577, 1578, 1586





ACPD
15, 1573–1615, 2015



Title Page
Abstract | Introduction
Conclusions | References
Tables | Figures
◂ | ▸
Back | Close
Full Screen / Esc
Printer-friendly Version
Interactive Discussion

Diehl, K., Simmel, M., and Wurzler, S.: Numerical sensitivity studies on the impact of aerosol properties and drop freezing modes on the glaciation, microphysics, and dynamics of clouds, J. Geophys. Res.-Atmos., 111, D07202, doi:10.1029/2005JD005884, 2006. 1577

Eidhammer, T., DeMott, P. J., Prenni, A. J., Petters, M. D., Twohy, C. H., Rogers, D. C., Stith, J., Heymsfield, A., Wang, Z., Pratt, K. A., Prather, K. A., Murphy, S. M., Seinfeld, J. H., Subramanian, R., and Kreidenweis, S. M.: Ice initiation by aerosol particles: measured and predicted ice nuclei concentrations versus measured ice crystal concentrations in an orographic wave cloud, J. Atmos. Sci., 67, 2417–2436, doi:10.1175/2010JAS3266.1, 2010. 1575

Field, P. R., Heymsfield, A. J., Shipway, B. J., DeMott, P. J., Pratt, K. A., Rogers, D. C., Stith, J., and Prather, K. A.: Ice in clouds experiment-layer clouds. Part II: Testing characteristics of heterogeneous ice formation in lee wave clouds, J. Atmos. Sci., 69, 1066–1079, doi:10.1175/JAS-D-11-026.1, 2012. 1575

Fridlind, A. M., Ackerman, A. S., McFarquhar, G., Zhang, G., Poellot, M. R., DeMott, P. J., Prenni, A. J., and Heymsfield, A. J.: Ice properties of single-layer stratocumulus during the Mixed-Phase Arctic Cloud Experiment: 2. Model results, J. Geophys. Res.-Atmos., 112, D24202, doi:10.1029/2007JD008646, 2007. 1578

Fukuta, N. and Takahashi, T.: The growth of atmospheric ice crystals: a summary of findings in vertical supercooled cloud tunnel studies, J. Atmos. Sci., 56, 1963–1979, doi:10.1175/1520-0469(1999)056<1963:TGOAIC>2.0.CO;2, 1999. 1590

Hartmann, S., Augustin, S., Clauss, T., Wex, H., Šantl-Temkiv, T., Voigtländer, J., Niedermeier, D., and Stratmann, F.: Immersion freezing of ice nucleation active protein complexes, Atmos. Chem. Phys., 13, 5751–5766, doi:10.5194/acp-13-5751-2013, 2013. 1574

Heymsfield, A. J. and Westbrook, C. D.: Advances in the estimation of ice particle fall speeds using laboratory and field measurements, J. Atmos. Sci., 67, 2469–2482, doi:10.1175/2010JAS3379.1, 2010. 1579

Hogan, R. J., Mittermaier, M. P., and Illingworth, A. J.: The retrieval of ice water content from radar reflectivity factor and temperature and its use in evaluating a mesoscale model, J. Appl. Meteorol. Clim., 45, 301–317, doi:10.1175/JAM2340.1, 2006. 1576

Illingworth, A. J., Hogan, R. J., O'Connor, E. J., Bouniol, D., Delanoë, J., Pelon, J., Protat, A., Brooks, M. E., Gaussiat, N., Wilson, D. R., Donovan, D. P., Baltink, H. K., van Zadelhoff, G.-J., Eastment, J. D., Goddard, J. W. F., Wrench, C. L., Haeffelin, M., Krasnov, O. A., Russchenberg, H. W. J., Piriou, J.-M., Vinit, F., Seifert, A., Tompkins, A. M., and Willén, U.: Cloudnet, B. Am. Meteorol. Soc., 88, 883–898, doi:10.1175/BAMS-88-6-883, 2007. 1576






ACPD

15, 1573–1615, 2015

Ice phase in altocumulus clouds over Leipzig

M. Simmel et al.

Meyers, M., DeMott, P., and Cotton, W.: New primary ice-nucleation parameterizations in an explicit cloud model, J. Appl. Meteorol., 31, 708–721, doi:10.1175/1520-0450(1992)031<0708:NPINPI>2.0.CO;2, 1992. 1575

Mitchell, D.: Use of mass- and area-dimensional power laws for determining precipitation particle terminal velocities, J. Atmos. Sci., 53, 1710–1723, doi:10.1175/1520-0469(1996)053<1710:UOMAAD>2.0.CO;2, 1996. 1578, 1579, 1589

Murray, B. J., O'Sullivan, D., Atkinson, J. D., and Webb, M. E.: Ice nucleation by particles immersed in supercooled cloud droplets, Chem. Soc. Rev., 41, 6519–6554, 2012. 1574

O'Sullivan, D., Murray, B. J., Malkin, T. L., Whale, T. F., Umo, N. S., Atkinson, J. D., Price, H. C., Baustian, K. J., Browse, J., and Webb, M. E.: Ice nucleation by fertile soil dusts: relative importance of mineral and biogenic components, Atmos. Chem. Phys., 14, 1853–1867, doi:10.5194/acp-14-1853-2014, 2014. 1575

Petzold, A., Fiebig, M., Flentje, H., Keil, A., Leiterer, U., Schroder, F., Stifter, A., Wendisch, M., and Wendling, P.: Vertical variability of aerosol properties observed at a continental site during the Lindenberg Aerosol Characterization Experiment (LACE 98), J. Geophys. Res.-Atmos., 107, 8128, doi:10.1029/2001JD001043, 2002. 1581

Phillips, V. T. J., DeMott, P. J., and Andronache, C.: An empirical parameterization of heterogeneous ice nucleation for multiple chemical species of aerosol, J. Atmos. Sci., 65, 2757–2783, 2008. 1575

Pospichal, B., Kilian, P., and Seifert, P.: Performance of cloud liquid water retrievals from ground-based remote sensing observations over Leipzig, in: Proceedings of the 9th International Symposium on Tropospheric Profiling, edited by: Cimini D., Di Girolamo P., Marzano F. S., and Rizi V., ISBN: 978-90-815839-4-7, doi:10.12898/ISTP9prc, L'Aquila, Italy, September 2012, Session C, 2012. 1576

Simmel, M., and Wurzler, S.: Condensation and activation in sectional cloud microphysical models, Atmos. Res., 80, 218–236, doi:10.1016/j.atmosres.2005.08.002, 2006. 1577

Sun, J., Ariya, P. A., Leighton, H. G., and Yau, M. K.: Modeling study of ice formation in warm-based precipitating shallow cumulus clouds, J. Atmos. Sci., 69, 3315–3335, doi:10.1175/JAS-D-11-0344.1, 2012. 1575

Westbrook, C. D., Hogan, R. J., and Illingworth, A. J.: The capacitance of pristine ice crystals and aggregate snowflakes, J. Atmos. Sci., 65, 206–219, doi:10.1175/2007JAS2315.1, 2008. 1579

**Table 1.** Overview of the model results for the dynamic sensitivity runs for the warmer case 1 (maximum values of L/IWMR: liquid/ice water mixing ratio, L/IWP: liquid/ice water path, CDN: cloud drop number, IPN: Ice particle number).

| run | parameter value differing from base case | LWMR $g\,kg^{-1}$ | IWMR $10^{-3}\,g\,kg^{-1}$ | LWP $g\,m^{-2}$ | IWP $10^{-3}\,g\,m^{-2}$ | CDN $cm^{-3}$ | IPN $L^{-1}$ |
|---|---|---|---|---|---|---|---|
| W_base | – | 0.277 | 0.304 | 41.33 | 62.27 | 46.89 | 0.0197 |
| W_h38 | $h_{bot} = 3800\,m$ | 0.332 | 0.329 | 57.05 | 73.11 | 48.63 | 0.0235 |
| W_h40 | $h_{bot} = 4000\,m$ | 0.225 | 0.286 | 28.58 | 58.12 | 61.48 | 0.0240 |
| W_h41 | $h_{bot} = 4100\,m$ | 0.170 | 0.259 | 18.23 | 45.81 | 59.53 | 0.0208 |
| W_w01 | $w_{ave} = 0.1\,m\,s^{-1}$ | 0.147 | 0.160 | 17.41 | 31.73 | 43.36 | 0.0138 |
| W_w02 | $w_{ave} = 0.2\,m\,s^{-1}$ | 0.232 | 0.241 | 32.86 | 47.18 | 54.57 | 0.0175 |
| W_w04 | $w_{ave} = 0.4\,m\,s^{-1}$ | 0.297 | 0.359 | 44.48 | 78.25 | 52.66 | 0.0219 |
| W_r1 | stoch. realiz. r1 | 0.261 | 0.254 | 40.32 | 54.85 | 64.26 | 0.0163 |
| W_r3 | stoch. realiz. r3 | 0.296 | 0.252 | 42.88 | 54.48 | 43.03 | 0.0167 |
| W_r4 | stoch. realiz. r4 | 0.269 | 0.197 | 40.91 | 46.93 | 47.42 | 0.0151 |





ACPD
15, 1573–1615, 2015

**Table 2.** Overview of the model results for the dynamic sensitivity runs for the colder case 2 (maximum values of L/IWMR: liquid/ice water mixing ratio, L/IWP: liquid/ice water path, CDN: cloud drop number, IPN: Ice particle number).

| run | parameter value differing from base case | LWMR $g\,kg^{-1}$ | IWMR $g\,kg^{-1}$ | LWP $g\,m^{-2}$ | IWP $g\,m^{-2}$ | CDN $cm^{-3}$ | IPN $L^{-1}$ |
|---|---|---|---|---|---|---|---|
| C_base | – | 0.215 | 0.026 | 29.35 | 10.71 | 70.56 | 0.462 |
| C_h70 | $h_{bot} = 7000\,m$ | 0.258 | 0.030 | 43.06 | 11.34 | 71.33 | 0.432 |
| C_h72 | $h_{bot} = 7200\,m$ | 0.169 | 0.022 | 18.71 | 10.11 | 90.51 | 0.396 |
| C_h73 | $h_{bot} = 7300\,m$ | 0.122 | 0.018 | 10.54 | 9.27 | 77.61 | 0.337 |
| C_w01 | $w_{ave} = 0.1\,m\,s^{-1}$ | 0.126 | 0.025 | 17.19 | 8.01 | 76.98 | 0.292 |
| C_w02 | $w_{ave} = 0.2\,m\,s^{-1}$ | 0.181 | 0.027 | 25.89 | 9.42 | 74.40 | 0.415 |
| C_w04 | $w_{ave} = 0.4\,m\,s^{-1}$ | 0.229 | 0.028 | 30.58 | 11.85 | 98.37 | 0.439 |
| C_r1 | stoch. realiz. r1 | 0.209 | 0.014 | 29.37 | 6.57 | 86.64 | 0.257 |
| C_r3 | stoch. realiz. r3 | 0.228 | 0.029 | 30.22 | 9.95 | 79.65 | 0.341 |
| C_r4 | stoch. realiz. r4 | 0.213 | 0.031 | 29.53 | 8.33 | 95.89 | 0.419 |





ACPD
15, 1573–1615, 2015

**Table 3.** Overview of the model results for the microphysical sensitivity runs for the warmer case 1 (maximum values of L/IWMR: liquid/ice water mixing ratio, L/IWP: liquid/ice water path, CDN: cloud drop number, IPN: Ice particle number).

| run | parameter value differing from base case | LWMR $g\,kg^{-1}$ | IWMR $10^{-3}\,g\,kg^{-1}$ | LWP $g\,m^{-2}$ | IWP $g\,m^{-2}$ | CDN $cm^{-3}$ | IPN $L^{-1}$ |
|---|---|---|---|---|---|---|---|
| W_in6 | $N_{AP,\ r>250\,nm} = 10^6\,kg^{-1}$ | 0.276 | 0.496 | 41.31 | 0.10 | 46.69 | 0.0296 |
| W_in7 | $N_{AP,\ r>250\,nm} = 10^7\,kg^{-1}$ | 0.276 | 0.801 | 41.24 | 0.17 | 41.61 | 0.0450 |
| W_col | ice shape: columns | 0.275 | 1.467 | 41.20 | 0.27 | 42.90 | 0.0257 |
| W_pla | ice shape: plates | 0.275 | 2.285 | 41.13 | 0.45 | 43.41 | 0.0267 |





ACPD
15, 1573–1615, 2015

**Table 4.** Overview of the model results for the microphysical sensitivity runs for the colder case 2 (maximum values of L/IWMR: liquid/ice water mixing ratio, L/IWP: liquid/ice water path, CDN: cloud drop number, IPN: Ice particle number).

| run | parameter value differing from base case | LWMR $\mathrm{g\,kg^{-1}}$ | IWMR $\mathrm{g\,kg^{-1}}$ | LWP $\mathrm{g\,m^{-2}}$ | IWP $\mathrm{g\,m^{-2}}$ | CDN $\mathrm{cm^{-3}}$ | IPN $\mathrm{L^{-1}}$ |
|---|---|---|---|---|---|---|---|
| C_in6 | $N_{\mathrm{AP},\ r>250\,\mathrm{nm}} = 10^6\,\mathrm{kg^{-1}}$ | 0.128 | 0.089 | 13.09 | 34.75 | 80.29 | 1.380 |
| C_in7 | $N_{\mathrm{AP},\ r>250\,\mathrm{nm}} = 10^7\,\mathrm{kg^{-1}}$ | 0.021 | 0.265 | 2.58 | 57.98 | 46.67 | 5.208 |
| C_col | ice shape: columns | 0.135 | 0.139 | 14.33 | 46.78 | 78.40 | 0.462 |
| C_col_in4 | ice shape: columns, $N_{\mathrm{AP},\ r>250\,\mathrm{nm}} = 10^4\,\mathrm{kg^{-1}}$ | 0.216 | 0.048 | 30.01 | 14.93 | 74.75 | 0.139 |
| C_pla | ice shape: plates | 0.104 | 0.183 | 9.94 | 57.11 | 39.41 | 0.472 |
| C_pla_in4 | ice shape: plates, $N_{\mathrm{AP},\ r>250\,\mathrm{nm}} = 10^4\,\mathrm{kg^{-1}}$ | 0.207 | 0.064 | 27.80 | 19.21 | 74.44 | 0.129 |





ACPD
15, 1573–1615, 2015

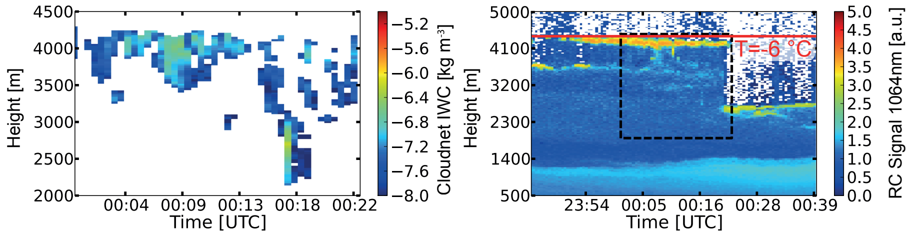


**Figure 1.** Lidar observations on 17 September 2011 (case 1). Left: ice water content IWC, right: range-corrected 1064 nm signal (in logarithmic scale, arbitrary units a. u.).





ACPD
15, 1573–1615, 2015

Ice phase in altocumulus clouds over Leipzig

M. Simmel et al.

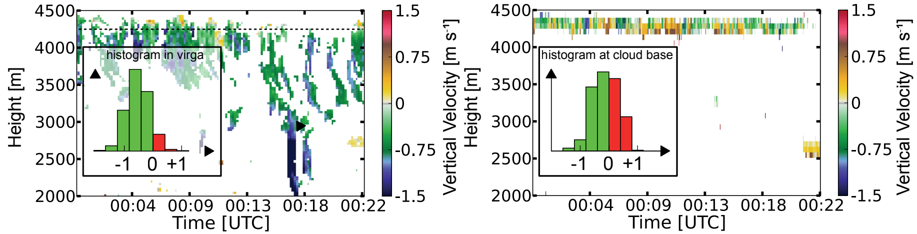


**Figure 2.** Vertical velocity for case 1. Left: derived from radar observations (valid for large particles; virgae), right: derived from lidar (valid for more numerous smaller droplets at cloud base).

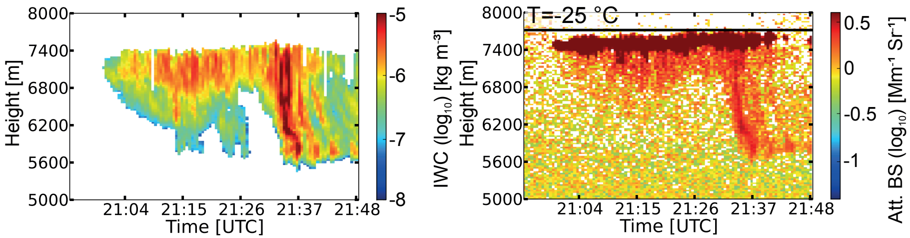


**Figure 3.** Lidar observations on 2 August 2012 (case 2). Left: ice water content IWC, right: 1064 nm attenuated backscatter coefficient.





ACPD
15, 1573–1615, 2015





Title Page
Abstract | Introduction
Conclusions | References
Tables | Figures
◀| |▶
◀ ▶
Back | Close
Full Screen / Esc
Printer-friendly Version
Interactive Discussion

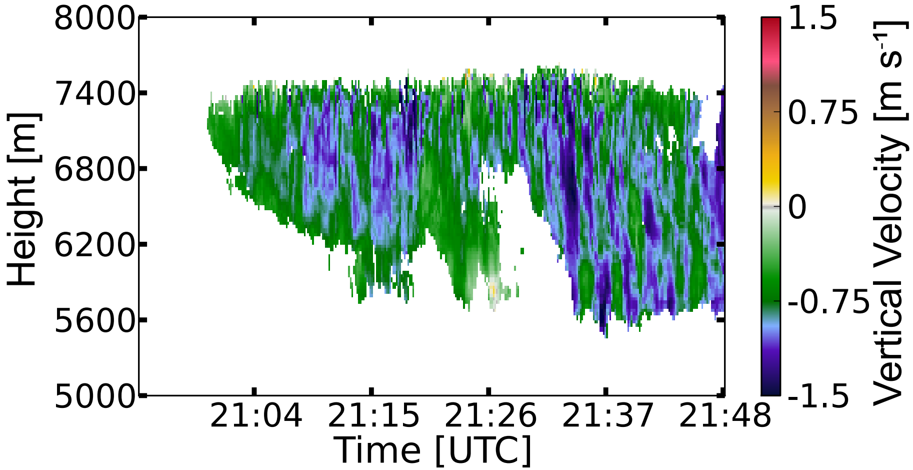


**Figure 4.** Vertical velocity for case 2, derived from radar observations.

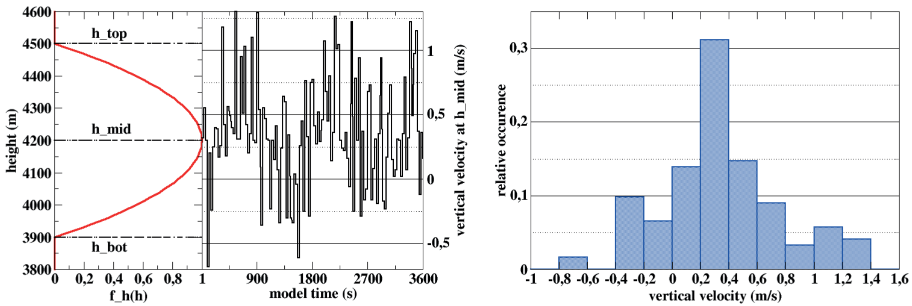


**Figure 5.** Vertical velocity field of the inner cylinder for case 1. Left: height dependence (red line) and temporal evolution of one realization of the stochastic vertical velocity field (black line) for $w_{ave} = 0.3\,\mathrm{m\,s^{-1}}$ at $h_{mid}$. Right: histogram of velocity field. Vertical velocity for case 2 is identical but for heights between 7100 and 7700 m.





ACPD
15, 1573–1615, 2015

Ice phase in altocumulus clouds over Leipzig

M. Simmel et al.

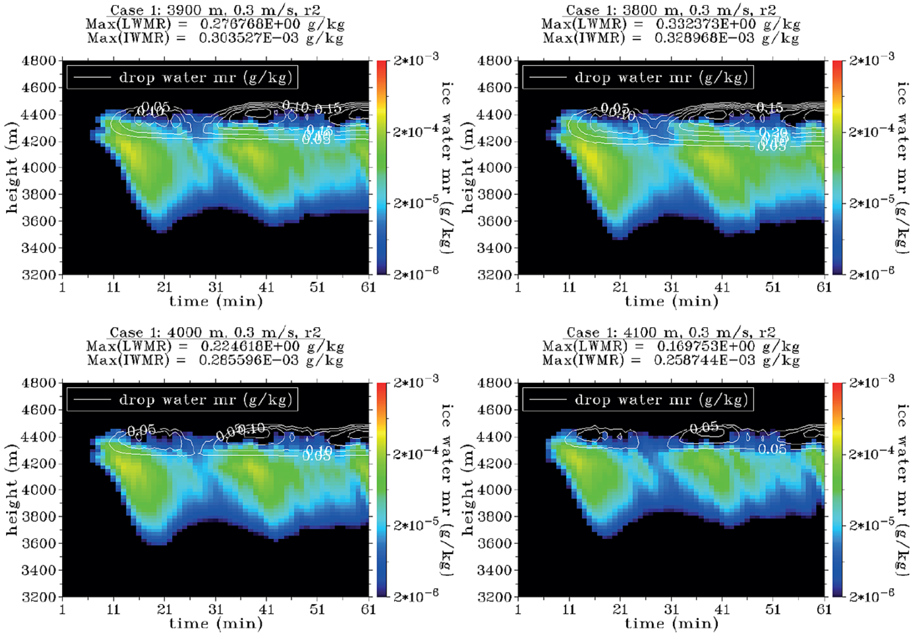


**Figure 6.** Liquid (contours) and ice water mixing ratio (colours, logarithmic scale) for case 1. Comparison of different values for $h_{bot}$ (upper left: W_base, $h_{bot}$ = 3900 m, upper right: W_h38, $h_{bot}$ = 3800 m, lower left: W_h40, $h_{bot}$ = 4000 m, lower right: W_h41, $h_{bot}$ = 4100 m).

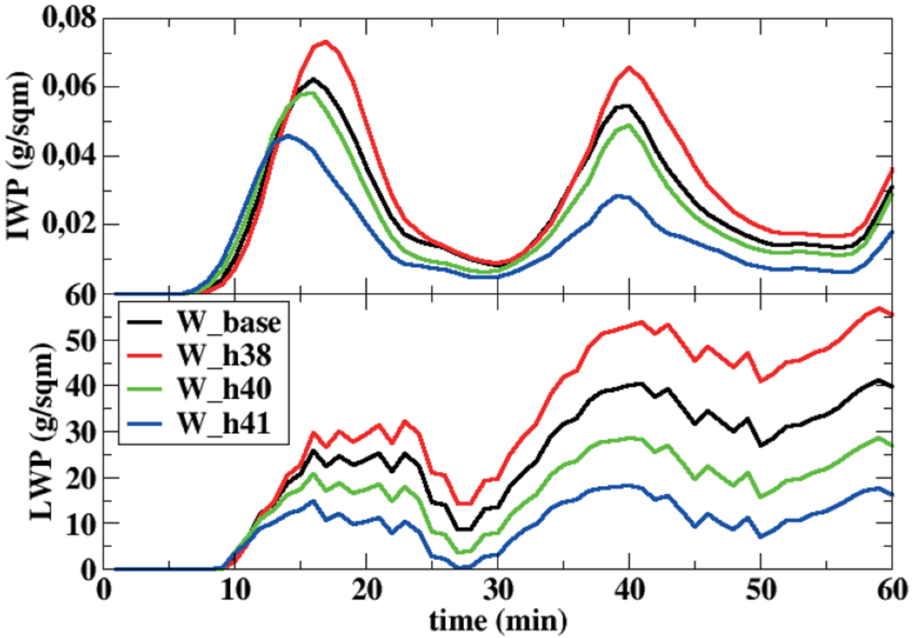


**Figure 7.** Liquid (lower panel) and ice water paths (upper panel) for case 1. Comparison of the different values for $h_{\text{bot}}$.

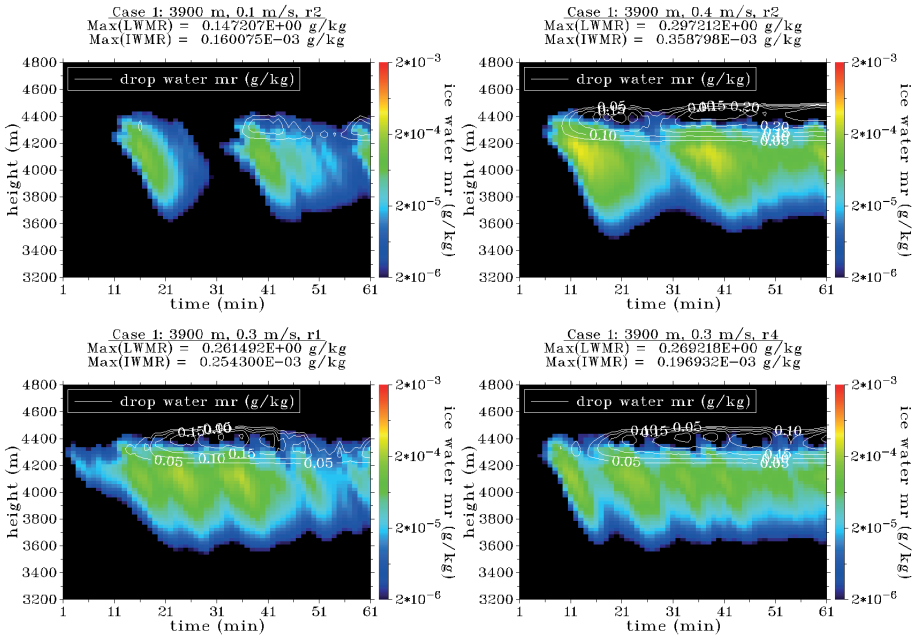


**Figure 8.** Liquid (contours) and ice water mixing ratio (colours, logarithmic scale) for case 1. Comparison of different average updraft velocities $w_{ave}$ (upper panel: left: W_w01, $w_{ave} = 0.1\,m\,s^{-1}$, right: W_w04, $w_{ave} = 0.4\,m\,s^{-1}$) and different stochastic realizations (lower: left: W_r1, r1, right: W_r4, r4).





ACPD
15, 1573–1615, 2015

Ice phase in altocumulus clouds over Leipzig

M. Simmel et al.

ACPD
15, 1573–1615, 2015





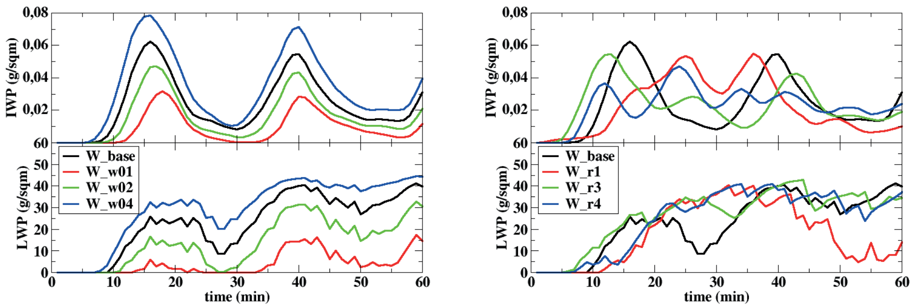


**Figure 9.** Liquid (lower panels) and ice water paths (upper panels) for case 1. Comparison of the different values for $w_{ave}$ (left) and the different stochastic realizations (right).

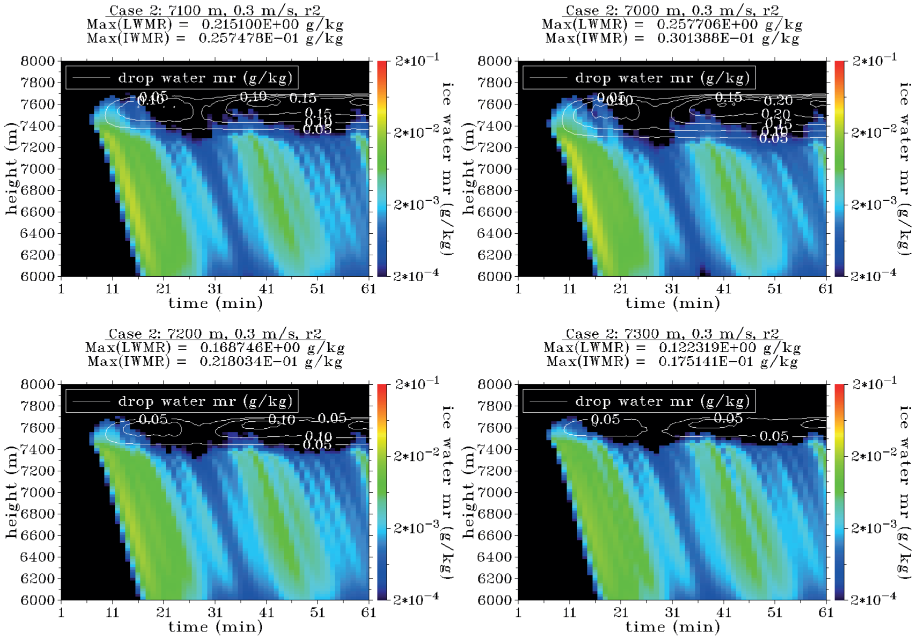


**Figure 10.** Liquid (contours) and ice water mixing ratio (colours, logarithmic scale) for case 2. Comparison of different values for $h_{bot}$ (upper left: C_base, $h_{bot}$ = 7100 m, upper right: C_h70, $h_{bot}$ = 7000 m, lower left: C_h72, $h_{bot}$ = 7200 m, lower right: C_h73, $h_{bot}$ = 7300 m).





ACPD
15, 1573–1615, 2015
Ice phase in altocumulus clouds over Leipzig
M. Simmel et al.

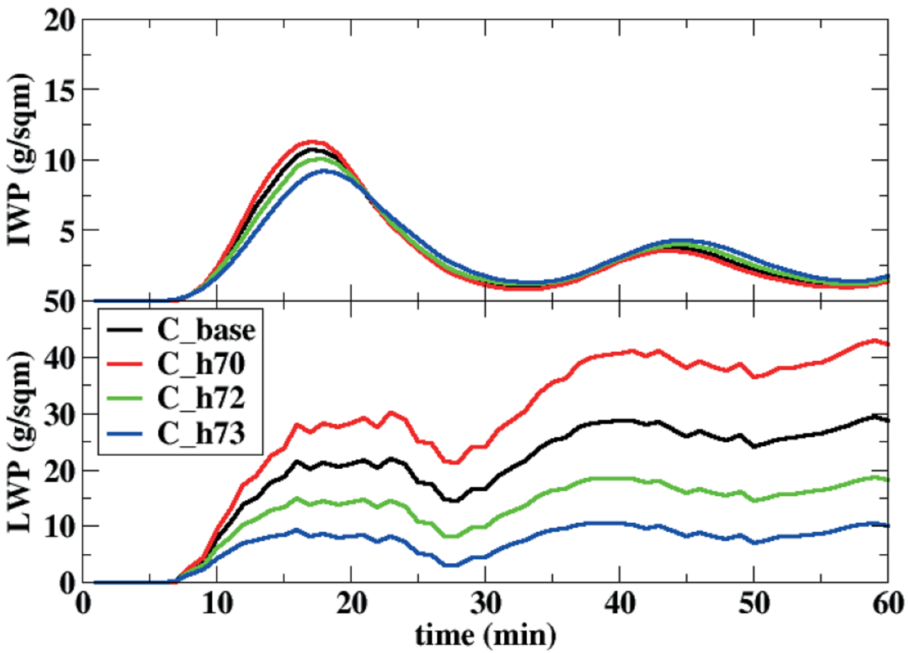


**Figure 11.** Liquid (lower panel) and ice water paths (upper panel) for case 2. Comparison of the different values for $h_{bot}$.





ACPD
15, 1573–1615, 2015

Ice phase in altocumulus clouds over Leipzig

M. Simmel et al.

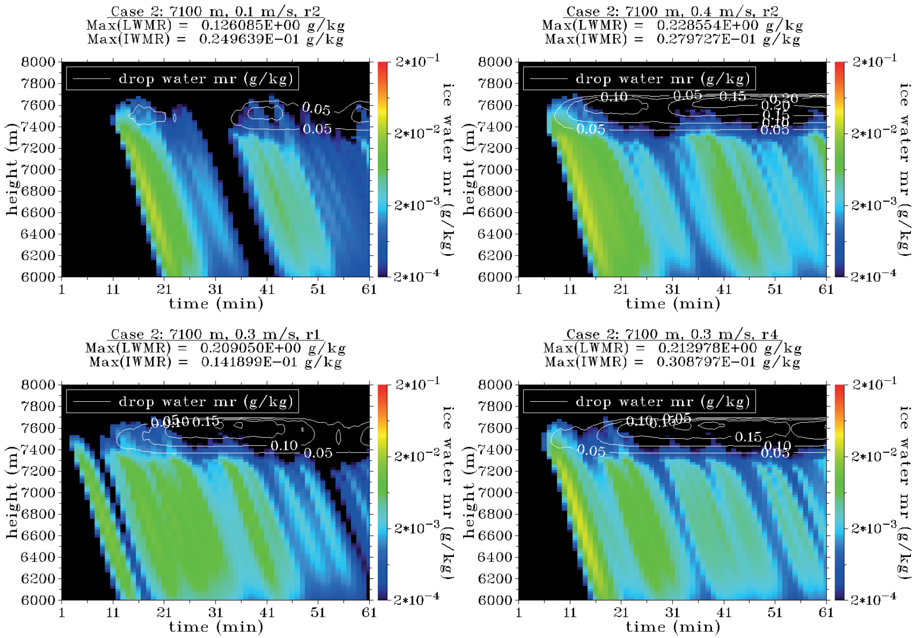


**Figure 12.** Liquid (contours) and ice water mixing ratio (colours, logarithmic scale) for case 2. Comparison of different average updraft velocities $w_{ave}$ (upper: left: C_w01, $w_{ave} = 0.1\,\mathrm{m\,s^{-1}}$, right: C_w04, $w_{ave} = 0.4\,\mathrm{m\,s^{-1}}$) and the different stochastic realizations (lower: left: C_r1, r1, right: C_r4, r4).





ACPD
15, 1573–1615, 2015

Ice phase in altocumulus clouds over Leipzig

M. Simmel et al.

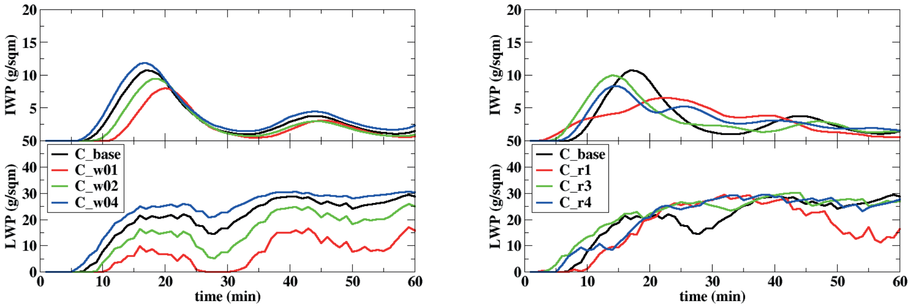


**Figure 13.** Liquid (lower panels) and ice water paths (upper panels) for case 2. Comparison of the different values for $w_{\text{ave}}$ (left) and the different stochastic realizations (right).





ACPD
15, 1573–1615, 2015

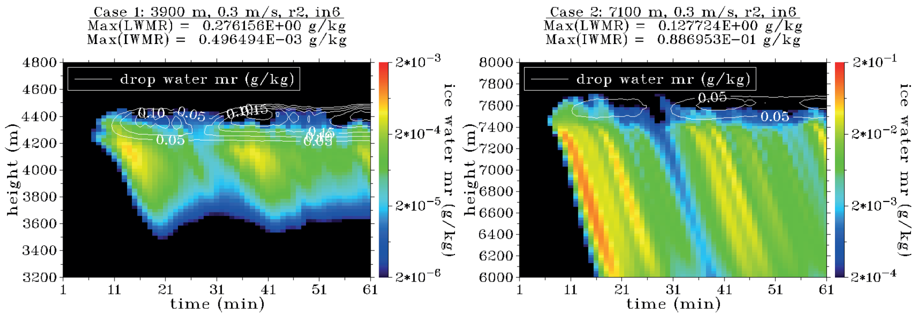


**Figure 14.** Liquid (colors) and ice water mixing ratio (contours, logarithmic scale) for case 1 (W_in6, left) and case 2 (C_in6, right). Enhancing IN by increasing $N_{\mathrm{AP},\, r>250\,\mathrm{nm}}$ by a factor of 10.





ACPD
15, 1573–1615, 2015

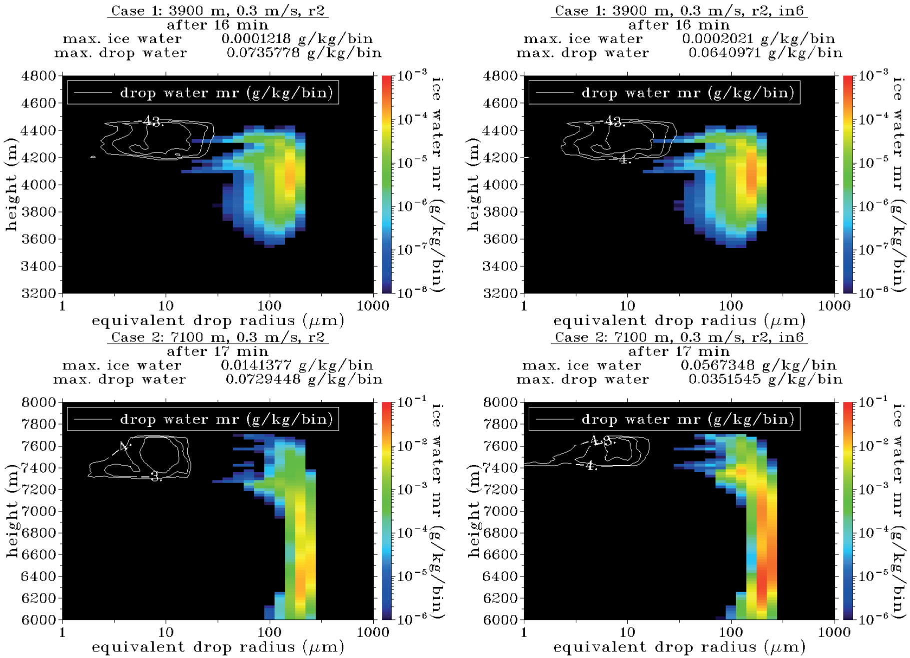


**Figure 15.** Liquid (colors) and ice water mass per bin (contours, logarithmic scale) for case 1 (upper panel) and case 2 (lower panel) for the respective base case (left) and the case with enhanced IN number (right; in6) after 16 and 17 min model time, respectively, corresponding to the IWP maximum of the base case runs.

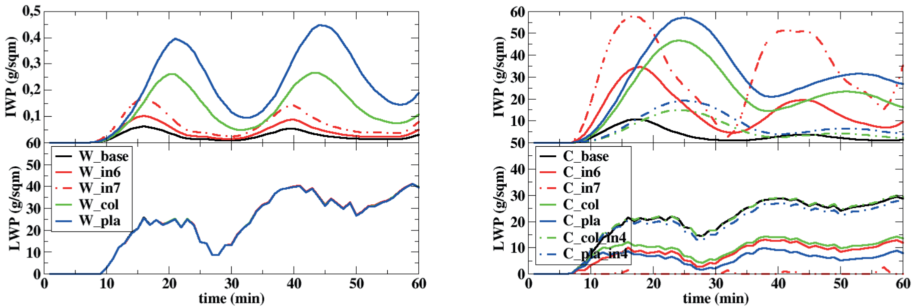


**Figure 16.** Liquid (lower panel) and ice water paths (upper panel) for case 1 (left) and case 2 (right). Comparison of the sensitivities with respect to IN number and ice particle shape.





ACPD
15, 1573–1615, 2015

Ice phase in altocumulus clouds over Leipzig

M. Simmel et al.

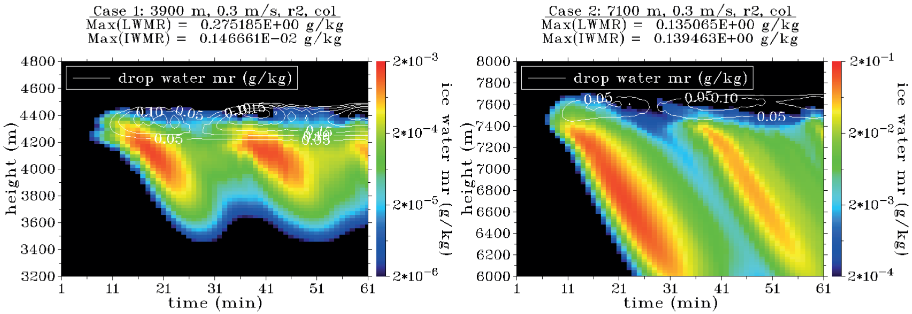


**Figure 17.** Liquid (colors) and ice water mixing ratio (contours, logarithmic scale). Results for changing ice particle shape to hexagonal columns for case 1 (W_col, left) and case 2 (C_col, right).





ACPD
15, 1573–1615, 2015

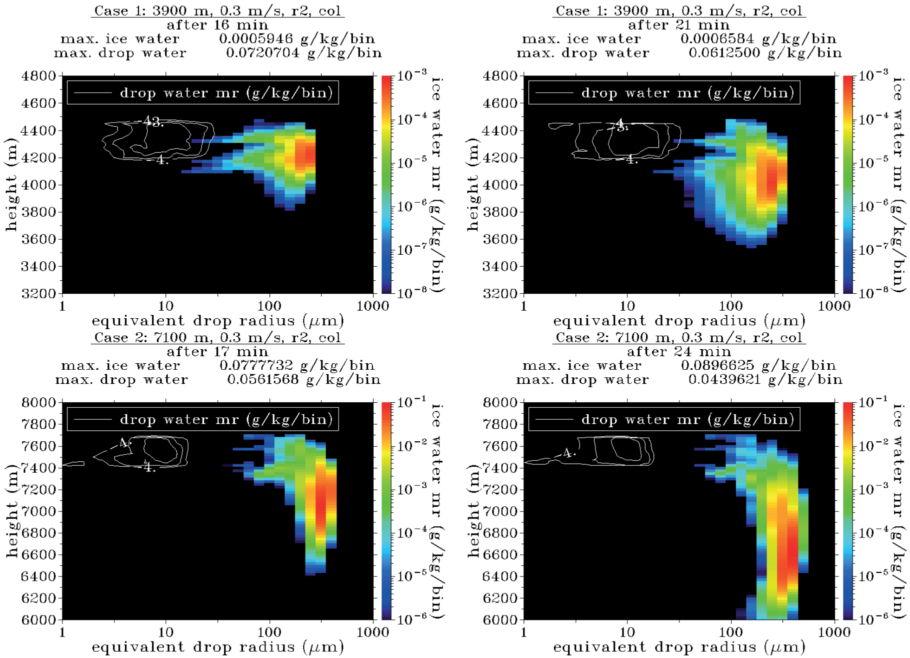


**Figure 18.** Liquid (colors) and ice water mass per bin (contours, logarithmic scale) for case 1 (upper panel) and case 2 (lower panel) assuming columns as ice particle shape at IWP maximum of the respective base case (left) and at IWP of the run (right).





ACPD
15, 1573–1615, 2015

Ice phase in altocumulus clouds over Leipzig

M. Simmel et al.